Article

Turbulent Eddy Generation for the CFD Analysis of Hydrokinetic Turbines

Matteo Gregori [1,2] [ID], **Francesco Salvatore** [1] [ID] **and Roberto Camussi** [2] [ID]

1   CNR-INM, National Research Council, Institute of Marine Engineering, Via di Vallerano, 139, 00128 Rome, Italy; matteo.gregori@inm.cnr.it, francesco.salvatore@cnr.it

2   Roma Tre University, Department of Engineering, Via della Vasca Navale 79, 00146 Rome, Italy; matteo.gregori@os.uniroma3.it, roberto.camussi@uniroma3.it

*   Correspondence: francesco.salvatore@cnr.it

Abstract: This paper presents a novel theoretical and computational methodology for the generation of an onset turbulent field with prescribed properties in the numerical simulation of an arbitrary viscous flow. The methodology is based on the definition of a suitable distribution of volume force terms in the right–hand side of the Navier–Stokes equations. The distribution is represented by harmonic functions that are randomly variable in time and space. The intensity of the distribution is controlled by a simple PID strategy in order to obtain that the generated turbulent flow matches a prescribed turbulence intensity. A further condition is that a homogeneous isotropic flow is established downstream of the region where volume force terms are imposed. Although it is general, the proposed methodology is primarily intended for the computational modelling of hydrokinetic turbines in turbulent flows representative of tidal or riverine installations. A first numerical application is presented by considering the injection of homogeneous and isotropic turbulence with 16% intensity into a uniform unbounded flow. The analysis of statistical properties as auto-correlation, power spectral density, probability density functions, demonstrates that the generated flow tends to achieve satisfactory levels of stationarity and isotropy, whereas the simple control strategy used determines overestimated turbulent intensity levels.

Keywords: tidal energy; hydrokinetic turbines; Synthetic turbulence models; computational fluid dynamics; Detached Eddy Simulation

1. Introduction

The hydrodynamic interaction between a fluid and a solid body moving through it is largely affected by the turbulence of the flow incoming to the body. By a simple observation, the turbulent nature of a flow is revealed by eddies with variable extension (lenght scale) and characteristic period (time scale). In terms of flow velocity, the eddies are responsible for a fluctuating component that can be assumed to perturb an onset smooth (laminar) flow. In contrast to the laminar flow that has a deterministic behaviour, turbulent fluctuations have a random nature.

Dealing with marine engineering problems, the impact of onset flow turbulence is of primary importance in the hydrodynamics of surface and underwater vehicles and of offshore structures. Typical examples for rotary-wing systems are the propellers that operate in the turbulent wake shed by the ship hull [1] or hydrokinetic turbines immersed in a tidal stream [2],[3]. In both cases, three main aspects of the interaction between rotating blades and the onset turbulent flow can be identified. Random fluctuations of the onset flow provoke the destabilization of the laminar boundary layer on the blade surface, and trigger the transition to turbulent boundary layer, which results into increased drag. Next, turbulent eddies with length and time scale compatible with rotor size and rotational speed, are responsible for the generation of fluctuating loads on rotor blades, with harmful effects in terms of vibrations and fatigue [4], [5], [6]. Not less important, the evolution of the wake

shed by rotor blades is largely affected by the intensity of the onset turbulent flow, with direct consequences on the performance of rotors operating in the wake of other rotors, as in the case of arrays of turbines [7].

Considering energy harvesting systems, an intrinsic problem lies in the difficulty to characterize the complexity of the turbulent stream in a tidal site [8], [9]. A variety of approaches exist in the literature on the modelling of onset flow turbulence in the Computational Fluid Dynamics (CFD) analysis of hydrokinetic turbines. Common to these methodologies is to develop computationally efficient approaches to generate a randomly fluctuating velocity field that interacts with the rest of the solution. A key difficulty is to obtain a simulated turbulent field with characteristics that are representative of real-life tidal flows. A recent review on the subject is proposed in [10]. Computational models for the generation of onset turbulent flows can be grouped into two main classes, precursor methods and synthetic methods. In the first case, a turbulent velocity field is injected into the computational domain by using experimental data or results from separate CFD modelling, notably by a DNS (Direct Navier–Stokes) solution. In the latter case, a suitable computational model is integrated into the CFD model in order to generate a flow velocity perturbation that satisfies statistical properties that are consistent with natural turbulent flows.

The methodology proposed in the present work falls within the broad class of synthetic methods. The turbulence generation model is intended for integration into a general purpose Navier–Stokes solver. The production of turbulent eddies is obtained through a volume force distribution defined as the combination of a harmonic distribution and a contribution that is randomly variable in time and space. The volume force terms are distributed in a narrow region of the computational domain, and the generated turbulent structures are shed downstream by the flow. Volume force modelling applied here grounds on authors' experience in the use of this type of methodology in the development of hybrid viscous/inviscid flow solvers for applications to ship propulsion [11] and tidal turbines [12], [13]. In order to match imposed values of flow turbulence, the intensity of volume force terms is iteratively updated by a suitable control strategy. The variance of the flow velocity components are taken as quantities observed by the control algorithm. In the present study, a simple Proportional-Integral-Derivative (PID) controller has been implemented. The proposed methodology is applied to a notional case study consisting of an unbounded uniform flow in which a prescribed level of turbulence intensity has to be generated. Turbulent flow simulations are performed by using the χnavis Navier–Stokes solver, in house developed at CNR-INM, and extensively validated for a variety of marine engineering problems [14]. Flow field simulations are performed by a Detached Eddy Simulation (DES) model. The abscence of perturbations in the simulated flow except for turbulence generation, allows to investigate in details the stationarity, homogeneity, isotropy properties of the established turbulent flow across the computational domain. This simple application represents the first step of an ongoing work aimed at the development of a computational methodology for the study of single turbines and arrays in turbulent flows representative of real tidal sites.

The manuscript is organized as follows. Main features of existing methodologies for the modelling of onset flow turbulence in CFD studies of tidal turbines are reviewed in Section 2. The proposed methodology is presented in Section 3, and details of the PID control strategy to enforce prescribed levels of turbulence intesity are given. The CFD model here applied for the analysis of tidal turbine flows is briefly reviewed in Section 4. The results of a numerical application to the simple case of an unbounded uniform flow with given onset flow turbulence intensity are presented and discussed in Section 5. Finally, conclusions and highlights on future work are commented in Section 6.

2. Review on turbulence generation methods

A review of the most popular methods used to generate an imposed turbulence intensity in the onset flow of a CFD simulation is presented. Turbulence generation

techniques addressed here are classified into precursor methods and synthetic methods. The latter includes the particular case of synthetic volume forcing methods, in which the methodology proposed in the present work can be grouped.

2.1. Precursor Methods (PM)

A simple approach to inject turbulence into a computational domain is to impose a velocity distribution that describes a fully developed turbulent field as inlet condition. The distribution can be derived from experimental data or generated by an independent computational analysis. In the latter case, the approach is sometimes referred to as *recycling method* as the analysis exploits the results of a preliminary (precursor) simulation. A classical example is the solution of the turbulent boundary layer on a flat plate. The resulting velocity profile is used to prescribe a velocity condition at the inlet of the domain or at some location inside of it (inflow zone). In this case a one-way (weak) coupling exists between the precursor calculation and the turbulent flow simulation of interest. Examples of weak coupling PM are presented in [15] and [16].

An alternative to weak coupling models consists in integrating the turbulence generation zone into the computational domain and analyze by a single simulation the production of turbulent structures and their evolution across the full computational domain. This approach is often indicated as strong coupling precursor model, see *e.g.*, [17] and [18]. Compared with weak coupling models, the strong coupling PM is in general characterized by a larger model complexity and computational effort.

2.2. Synthetic Methods (SM)

Synthetic Methods (SM) exploit the assumption that a turbulent flow can be considered as the superposition of a baseline laminar flow $\overline{\mathbf{u}}$ and a randomly fluctuating velocity field $\mathbf{u}'$ (Reynolds decomposition)

$$\mathbf{u}(\mathbf{x}, t) = \overline{\mathbf{u}}(\mathbf{x}, t) + \mathbf{u}'(\mathbf{x}, t). \tag{1}$$

A typical approach to model the velocity perturbation $\mathbf{u}'$ is to introduce a noise function defined as the convolution between a random signal $\mathbf{r}$ and a suitable filtering function $\mathbf{w}$. For a one-dimensional (1D) problem, the filter can be written as (see *e.g.*, [19])

$$u'_m = \sum_{n=-N}^{N} w_n r_{n+m} \tag{2}$$

where $2N + 1$ is the number of the samples of u.

Following [20], the extension to a three-dimensional (3D) flow problem can be simply obtained by combining 1D filters defined in each direction, as $w(x, y, z) = w_x(x)w_y(y)w_z(z)$, for an arbitrary point $\mathbf{x}$ with coordinates (x, y, z). In few studies, analytical derivations have been proposed to determine the filtering coefficients of desired correlation functions. This technique is referred to as Synthetic Digital Filtering Method (SDFM).

A more widely used approach consists in projecting the randomly fluctuating velocity component onto a suitable basis of harmonic functions. A typical example is the following representation by a truncated Fourier series (Synthetic Random Fourier Method, SRFM). Applications of the SRFM are described in [21]. [22] and [10]. For a given energy spectrum E, the amplitude of the fluctuating velocity vector in the wave field associated to the vector $\mathbf{k}_n$ can be specified. A three-dimensional decomposition of this field can be written as

$$u'(\mathbf{x}, t) = 2 \sum_{n=1}^{N} \hat{u}_n(t) \cos\left(\mathbf{k}_n \cdot \mathbf{x} + \psi_n(t)\right) \gamma_n \tag{3}$$

where ψ_n denote random phases associated with the $\mathbf{k}_n$ vector, γ_n is the unit vector normal to $\mathbf{k}_n$ and N is the number of samples. Following [23], it can be easily shown that the

amplitudes $\hat{u}_n(t)$ are associated to the turbulent kinetic energy that is introduced into the flow.

2.3. Synthetic Volume Forcing Methods (SVFM)

Computational approaches based on PM and SM have in common that a turbulent velocity field is obtained by combining a baseline flow with a velocity perturbation that is simply injected to the flow (PM approach) or superimposed to it (SM approach). A limitation of these approaches is about the consistency of the resulting flow field as a solution of the Navier–Stokes equations. In particular, dealing with SM approaches dedicated modelling is required to ensure that the fluctuating velocity distribution preserves the divergence–free condition of an incompressible baseline flow. The problem is addressed and a solution is proposed in [24]. Similarly, the consistency of spatial and temporal correlations in PM and SM solutions with those measured in real turbulent flows is often a point of concern.

Completely different assumptions are at the basis of the so-called Synthetic Volume Forcing Methods (SVFM). The idea is that volume force terms can be introduced in selected regions of the computational domain to generate a flow field perturbation that results into the development of turbulent structures downstream of the generation region.

The use of the volume force terms is quite general in CFD, with many different applications. Gravity forces in a free-surface flow problem are an example of volume forces. The concept can be generalized to represent the effect of a physical obstacle to the surrounding flow. The description of the obstacle as a solid boundary of the fluid domain is replaced by suitable distributions of volume force terms that reproduce the flow perturbation generated by the obstacle. The intensity of volume force terms is a problem unknown and computational approaches specific to the problem of interest have been proposed. Examples of volume force techniques for the computational analysis of the interaction of screw propellers with the viscous flow around a ship hull are presented, *e.g.*, in [25,26], and [11]. An application of volume force methods to the hydrodynamic analysis of single hydrokinetic turbines and arrays is presented in [12]. In [27] a theoretical analysis on volume force models is presented and alternative approaches are described by assuming linear anisotropic forcing term distributions. Other applications of SVFM are given in [28] and [29].

Dealing with the generation of turbulent structures in a baseline flow, volume force techniques can be used to develop digital models of the so-called *turbulence grids* used in the experimental field. A typical approach to generate turbulence in a wind tunnel or in a water flume consists in the installation of wire grids upstream of the test section area of interest. For a given onset flow, the wakes shed by grid elements produce turbulent flows whose intensity and other characteristics depend on grid geometry parameters as wire section, shape, size and spacing. Rigid (or *passive*) grids are designed to generate a given turbulent intensity level. Larger flexibility can be obtained with *active* grids in which free or controlled moving objects are integrated in order to stimulate the generation of eddies with different space and time scales. The application of passive and active grids is discussed, *e.g.*, in [30]. To some extent, the variability of turbulent scales can be also achieved by the so-called *fractal* passive grids characterized by the superposition of a basic texture element reproduced with different scales. Examples of passive fractal and active grids are shown in Fig. 1.

Compared with PM and SM approaches reviewed above, SVFM has the main advantage that both velocity and pressure perturbations associated with the turbulence generation mechanism are fully consistent with the numerical solution describing the flow field in the computational domain. In particular, an incompressible baseline flow remains divergence–free also if strong turbulence eddies are generated. However, particular attention is required to demonstrate the capability of a volume force distribution to generate a perturbation field with statistical properties in accordance with real turbulent flow metrics.
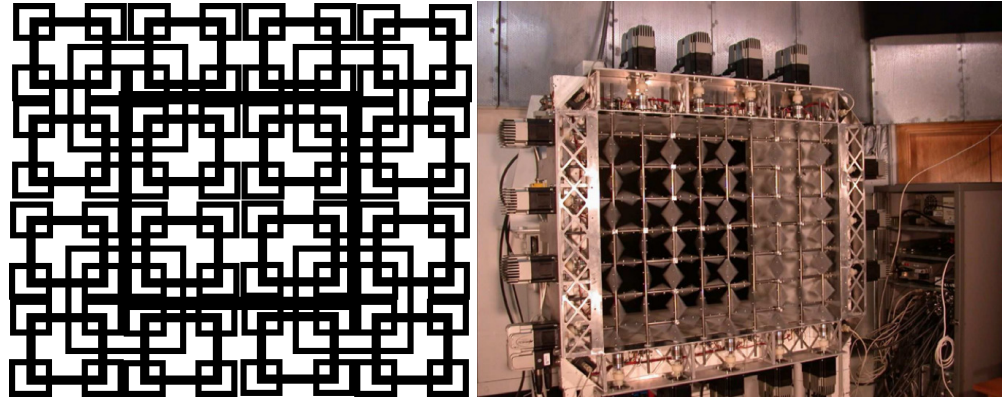
Figure 1. Examples of a passive fractal grid (left, from [30]) and of an active grid (right, from [30]) used in wind tunnel experiments.

An interesting study on this subject is presented in [31], where the characteritics of the turbulent flow generated by a single bar in a grid is investigated in details.

The methodology proposed in the present work falls within the class of SVFM approaches. The volume force distribution is defined as the combination of a harmonic distribution and a contribution that is randomly variable in time and space. The intensity of the volume force terms is iteratively updated by a PID controller in order to match imposed values of turbulence intensity in selected regions downstream of the turbulence generation area.

3. Turbulence production and control methodology

The present formulation is derived for an incompressible turbulent viscous flow. The classical Reynolds decomposition of the velocity field $\mathbf{u} = \mathbf{u}(\mathbf{x}, t)$ into mean $\overline{\mathbf{u}}(\mathbf{x}, t)$ and randomly fluctuating term $\mathbf{u}'(\mathbf{x}, t)$ is used, see Eq. (1). A similar decomposition holds for the pressure p. In the following, the overbar symbol $\overline{(\ \ )}$ will be omitted for mean quantities unless necessary to avoid confusion.

For the sake of clarity, a 3D–space Cartesian orthogonal frame of reference $(Ox_1x_2x_3)$ and unit vectors $\mathbf{e}_i (i = 1, 2, 3)$ are considered. The unperturbed (baseline) flow is uniform and directed along the x_1 axis, that is, $\mathbf{u} = u_\infty \mathbf{e}_1$. In the following, x_1 will be referred to as the *streamwise* direction. Assuming a generic volume force distribution $\mathbf{f} = \mathbf{f}(\mathbf{x}, t)$ exists in the fluid domain, mass and momentum equations can be written in Cartesian components and non-dimensional form as

$$\begin{cases} \partial_i u_i = 0 \\ \partial_t u_i + u_i \partial_j u_i = -\partial_i p + \partial_j T_{ij} + f_i \qquad (i = 1, 2, 3) \end{cases}$$

where $u_i = \mathbf{u} \cdot \mathbf{e}_i$ and $f_i = \mathbf{f} \cdot \mathbf{e}_i$ and p is the pressure. A compact notation is used, with symbols ∂_i, ∂_t denoting, respectively, derivation with respect to coordinate x_i and time t, whereas repeated indices denote summation. Quantities T_{ij} denote the components of the stress tensor

$$T_{ij} = \frac{1}{Re}(\partial_j u_i + \partial_i u_j), \tag{4}$$

where Re is the Reynolds number.

Following the SVFM concept, the forcing terms f_i in the right–hand side of the momentum equation is responsible for the generation of a flow perturbation. In order to have a fully general volume force distribution, the components of vector $\mathbf{f}$ will depend on both time and space, that is

$$f_i = f_i(x_1, x_2, x_3, t) \qquad (i = 1, 2, 3) \tag{5}$$

Recalling the classification of turbulence grids used in the experimental field in Section 2.3, a definition of quantity **f** that generalizes in a digital fashion the concept of fractal passive and active grids is proposed here. The volume force distribution combines the following contributions:

- **f**^{H}, a spatially harmonic and constant in time deterministic sine distribution, with given wavelenght λ,
- **f**^{RH}, a randomly fluctuating harmonic distribution obtained by introducing at each time in **f**^{H} a random variation of the sine phase, and a spatially random perturbation of the intensity.

The volume force terms f_i are non-zero within a flow region denoted as the *generation volume* $\mathcal{V}_g$. This region is represented by a box with edges aligned to the x_i directions. Within this volume, quantities f_i are assumed to be constant in the x_1 direction, whereas in the (x_2, x_3) plane, one has

$$f_i^H(x_2, x_3) = \sum_{k=1,N_k} \left[\sin\left(2\pi\lambda_k x_2\right) + \sin\left(2\pi\lambda_k x_3\right) \right] \qquad (i = 1, 2, 3) \qquad (6)$$

where N_k is a prescribed number of harmonic terms and λ_k the wavelenghts associated to each term. A sample f_i^H distribution obtained from Eq. (6) with $N_k = 1$ is depicted in Fig. 2. It should be noted that distributions with $N_k > 1$ can be used to mimic fractal passive grids, left Fig. 1. Next, denoting by $\psi'(t)$ and $\psi''(t)$ two independent pseudo random
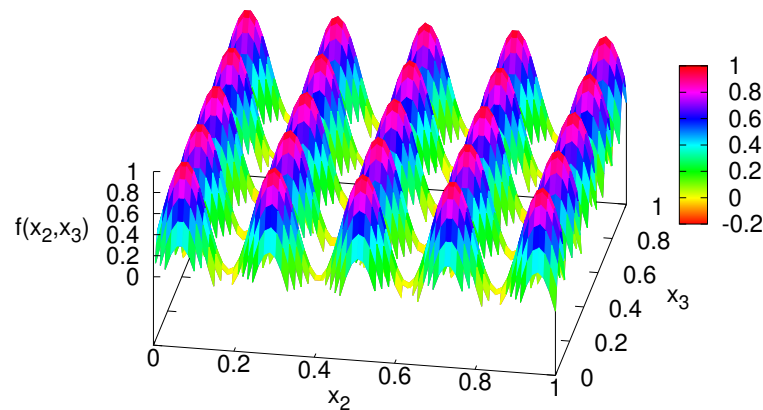

Figure 2. Sample harmonic distribution of volume force terms from Eq. (6) ($N_k = 1$).

functions, a non-deterministic phase shift is introduced in the sine terms in Eq. (6). A further noise contribution is introduced by summing to f_i^H a spatially random perturbation $W = W(x_2, x_3, t)$. Quantities ψ', ψ'' and W are built from a constant probability density function that generates pseudo random values in the range $[0:1]$. The obtained values are further scaled to have ψ', ψ'' in the range $[-\pi : \pi]$, and W in the range $[-1 : 1]$. This allows to introduce a random variability of both position and intensity of the perturbation by the volume forces.

The resulting distribution reads

$$f_i^{RH}(x_2, x_3, t) = C_1 \sum_{k=1,N_k} \sin\left(2\pi\lambda_k x_2 + \psi'(t)\right) + \sin\left(2\pi\lambda_k x_3 + \psi''(t)\right)$$
$$+ W(x_2, x_3, t) \quad (i = 1, 2, 3) \qquad (7)$$

By definition, W values at distinct points $\mathbf{x}_a, \mathbf{x}_b$ or time instants t_a, t_b have zero correlation.

The constant C_1 in Eq. (7) is used to normalise the volume force intensity in the range $[-1:1]$. An example of the distribution obtained by Eq. (7) with $N_k = 1$ is depicted in Fig. 3. At different time instants, the intensity and position of crests and troghts changes and a random de-syncronization of flow perturbation sources is achieved. Such a volume force distribution can be taken as representative of an active physical grid, right Fig. 1. The
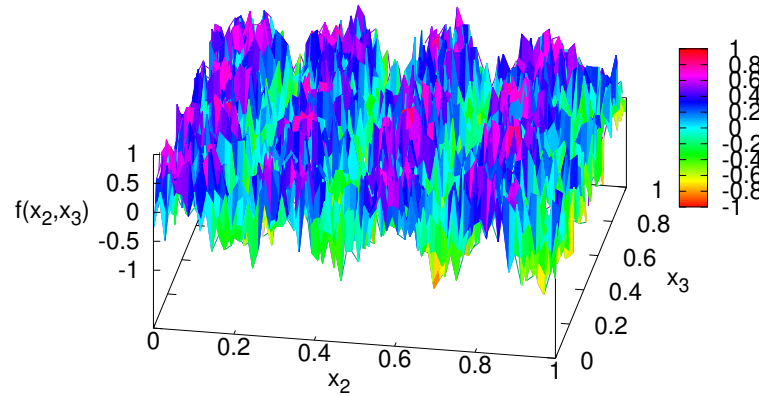

Figure 3. Sample harmonic distribution of volume force terms with phase and intensity random noise from Eq. (7) ($N_k = 1$).

variation of $f_i^{RH}(\mathbf{x}, t)$ in the direction x_1, is given by the attempt to simulate the thickness of a real grid. Then we introduce the box function (rect function) as $\Pi_{x_1^{(1)}, x_1^{(2)}}(x_1)$, to produce a function that is zero everywhere except to the points where the grid would be located, thus going to simulate the thickness of the same. We can define this function as follows:

$$\Pi_{x_1^{(1)}, x_1^{(2)}}(x_1) = H(x_1 - x_1^{(1)}) - H(x_1 - x_1^{(2)}) \tag{8}$$

and more precisely we are going to identify the values like this:

$$\Pi_{x_1^{(1)}, x_1^{(2)}}(x_1) = \begin{cases} 0, & x_1 < x_1^{(1)} \\ 1, & x_1^{(1)} < x_1 < x_1^{(2)} \\ 1/2, & x_1 = x_1^{(1)}, x_1^{(2)} \\ 0, & x_1 > x_1^{(2)} \end{cases} \tag{9}$$

Now this function can multiply the relationship constructed in Eq. (7) to create $f_i^{RH}(x_1, x_2, x_3, t)$:

$$f_i^{RH}(x_1, x_2, x_3, t) = \Pi_{x_1^{(1)}, x_1^{(2)}}(x_1) f_i^{RH}(x_2, x_3, t) \tag{10}$$

With this definition, the volume force distribution is assumed to be constant in the streamwise direction x_1 within a given generation volume $\mathcal{V}_g$ and zero outside. The effect of the streamwise extension of this region on the perturbation generated by the volume forces has been discussed in [32].

3.1. Turbulent flow metrics

For applications to engineering problems, it is fundamental to ensure that the volume force distribution defined in Eq. (7) is able to generate a flow field perturbation whose statistical properties are representative of prescribed flow conditions. This is the case of the analysis of hydrokinetic turbine performance in a given deployment site. The

high-fidelity modelling of turbine operation implies that the turbulent intensity and other characteristics of the onset flow in the site are adequately accounted for in the simulations. The extraordinary complexity of turbulent flows can be partially characterized through the definition of a dedicated metrics. A discussion on this aspect can be found *e.g.*, in [33]. A primary characterization of a turbulent flow is achieved by analyzing the correlation between fluctuating velocity components. Considering different points at a given time, the spatial correlation tensor is defined as

$$R_{ij}(\mathbf{r}) \;=\; E\Big[u_i'(\mathbf{x})\,u_j'(\mathbf{x}+\mathbf{r})\Big] \tag{11}$$

where the symbol $E[\,]$ denotes the expected value operator, and $\mathbf{r}$ is an arbitrary position vector with origin in $\mathbf{x}$. Similarly, the temporal correlation tensor at a given point reads $R_{ij}(\tau) = E[u_i'(t)\,u_j'(t+\tau)]$, where τ is and arbitrary positive or negative time delay from time t. For $\mathbf{r}=0$ or $\tau=0$, the quantity $R_{ij}(0)$ equals the Reynolds stress tensor.

By introducing the variance of the turbulent flow in the i–th direction as $\sigma_i^2 = E[u_i'\,u_i']$, simple manipulations show that a direct relationship exists between the trace of tensor $R_{ij}(0)$ and the variance

$$\mathrm{Tr}(R_{ij}(0)) \;=\; R_{11}(0) + R_{22}(0) + R_{33}(0) \;=\; \sum_{i=1}^{3}\sigma_i^2 \tag{12}$$

where the symbol $\mathrm{Tr}(\;)$ denotes the trace operator.

A definition of the turbulent intensity I_∞ is then given as

$$I_\infty \;=\; \frac{1}{u_\infty}\sqrt{\sum_{i=1}^{3}\sigma_i^2} \tag{13}$$

In particular, under homogeneous isotropic turbulence assumptions, one has $\sigma_1^2 = \sigma_2^2 = \sigma_3^2$. Recalling Eq. (13), turbulence intensity and variance $\sigma^2 = \sigma_i^2\ (i=1,2,3)$ are mutually dependent parameters

$$I_\infty \;=\; \frac{1}{u_\infty}\sqrt{3\sigma^2} \qquad\qquad \sigma^2 \;=\; \frac{1}{3}\,u_\infty^2\,I_\infty^2. \tag{14}$$

3.2. Generated turbulence control strategy

A key feature of the proposed methodology is that the volume force distribution in Eq. (7) can be dynamically modified in order to ensure that the generated turbulent flow matches imposed conditions of the turbulence intensity. This is obtained by combining the numerical solution of equations (4) with a control algorithm that updates the intensity of the volume force term $\mathbf{f}$ to enforce the realization of target flow properties. To this purpose, a simple control strategy based on a standard Proportional-Integral-Derivative (PID) controller is applied here.

Recalling the direct relationship between turbulence intensity I_∞ and variance associated to the velocity components, $\sigma_i^2\ (i=1,2,3)$ in Eq. (13), the latter quantities are observed by the control algorithm. Assuming the objective is a homogeneous and isotropic turbulent flow, the variance is equal in all directions and Eq. (14) can be used to determine a unique relationship between the desedered turbulence intensity $I_{\infty,des}$ and the desired variance σ_{des}^2.

For an arbitrary distribution of volume force terms, the flow field solution will determine variance terms σ_i^2 that do not match the desired conditions. The following error functions $\mathcal{E}_i$ can be defined

$$\mathcal{E}_i \;=\; \left(\sigma_{des}^2 - \sigma_i^2\right)/\sigma_{des}^2 \qquad (i=1,2,3). \tag{15}$$

The minimization of the error functions above is obtained by the PID control with parameters k_i, $(i = 1, 2, 3)$ defined as follows

$$k_i(t) \;=\; a_{1\,i}\mathcal{E}_i(t) \;+\; a_{2\,i}\int_{t_0}^{t}\mathcal{E}_i(t)dt \;+\; a_{3\,i}\partial_t\mathcal{E}_i(t) \qquad (i = 1, 2, 3) \qquad (16)$$

where $t_0 < t$, and the coefficients $a_{1\,i}, a_{2\,i}, a_{3\,i}$ define, respectively, the proportional, integral and derivative control parameters for the i–th velocity component.

Quantities $k_i(t)$ are used to force variations of the intensity of volume force terms by a simple proportionality relation. The expression in Eq. (7) is recast as

$$f_i^{RH}(\mathbf{x}, t) \;=\; k_i(t)\,\Pi(x_1)\,f_i^{RH}(x_2, x_3, t) \qquad (i = 1, 2, 3) \qquad (17)$$

The PID control interacts with the numerical solution of the Navier–Stokes equations through an iterative procedure as sketched in the flow chart in Fig. 4.
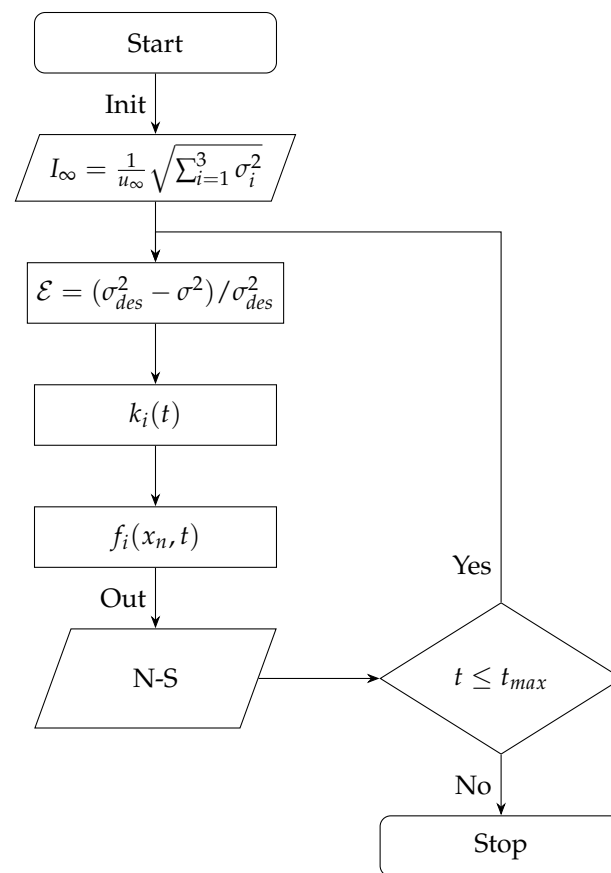

Figure 4. Iterative turbulence intensity control procedure.

4. Computational model

The analysis of the turbulent flow generation is addressed through the numerical solution of Eqs. (4) by a Detached Eddy Simulation (DES) approach. A convection–diffusion equation is solved whit production and destruction terms and a forcing function that depends on the distance from solid walls. At large distance from a solid boundary, the equation reduces to a Large Eddy Simulation (LES) closure model, see [14] for details.

Numerical solutions are obtained by the Navier-Stokes solver χ–*Navis*, in-house developed at CNR-INM and extensively validated for a wide range of applications on hydrodynamics studies of marine vehicles and offshore structures. The solver is based on a finite volume technique with pressure and velocity co-located at cell centers. For the viscous terms a standard second order centered scheme is adopted, whereas for the

inviscid part a fourth order centered scheme is used. The formal spatial accuracy of this method is second-order (owing to the treatment of the viscous terms). Nevertheless, the use of a less dissipative scheme for the convective terms allows to follow the formation and convection of strong gradients for a considerably longer distance than with the use of a second order-scheme. The convergence ratio for the inner iteration is accelerated by means of local time stepping, an implicit Euler scheme with approximate factorization and a multi-grid technique. The computational domain is discretized by a structured multi-block mesh. Overlapping among grid blocks is made possible by a Chimera technique [34]. More details on the numerical model can be found in [35].

5. Numerical application

The capability of the proposed methodology to generate turbulent eddies with imposed metrics in an arbitrary onset viscous flow is analysed here through a simple application. The proposed case study deals with the generation of homogeneous isotropic turbulence with given intensity I_∞ into a uniform unbounded flow with constant velocity u_∞, hereafter referred to as the *nominal* flow speed. First, the computational set-up is described. Next, the results of the flow field simulation are presented and discussed.

5.1. Computational set-up

The computational domain is a cylinder with the two bases representing the inlet and outlet sections, with the cylinder axis aligned with the direction of the unperturbed flow (streamwise direction). Denoting by L a reference length, the cylinder has length $26L$ and radius $9L$. These dimensions are compatible with the set-up for the simulation of the flow field around an isolated horizontal-axis turbine with diameter $D = L$.

A parallelepipedal grid block defines the control volume where turbulence is generated (*generation* block). This block is centred at distance $d_g = 14L$ from the inlet section, and is $0.05L$ long in the streamwise direction and $1.4L \times 1.4L$ wide in the normal directions. Downstream of it, another parallelepipedal grid block defines the flow region where the generated turbulence is monitored and statistical properties are evaluated (*control* block). This block is $2.0L$ long in the streamwise direction and $1.3L \times 1.3L$ wide in the normal directions. These two blocks are immersed into a background grid formed by a toroidal block extended to the external boundary of the computational domain (*background* block) and internally limited by a thin cylindrical gap that is filled with two partially overlapping parallelepipedal blocks extended from the centre of the domain to the inlet and to the outlet sections (*filling* blocks). Dimensions and number of cells of each block are given in Table 1. The discretization refers to the finest grid level, whereas the multi-grid algorithm uses refinement levels, with the coarser grid obtained by removing every second point from the finer grid. In the present study, preliminary results with only 2 grid refinement levels are presented. A total of 5 blocks and approximately 2×10^6 cells on the finest grid level is obtained. Grid node stretching is applied in background and filling blocks with cells

Block	L_1/L	L_2/L	L_3/L	Cells
Generation	0.05	1.4	1.4	$48 \times 128 \times 128$
Control	2.0	1.3	1.3	$700 \times 128 \times 128$
Background	26.0	9.0 (radius)	–	$360 \times 60 \times 90$

Table 1. Computational grid: main blocks size L_i in the i–wise direction ($i = 1, 2, 3$), and number of cells on the finest level.

clustering in the flow region downstream of the turbulence generation area, while no stretch is applied on both generation and control blocks to avoid local grid refinement effects on the calculated turbulence metrics. Figure 5 presents views of the overall computational domain and details of the generation and control blocks. It can be noted that the generation block is relatively thin in the streamwise direction, whereas the control block covers a large

portion of the flow field. A velocity condition $\mathbf{u} = u_\infty \mathbf{e}_1$ is imposed at the inlet section.
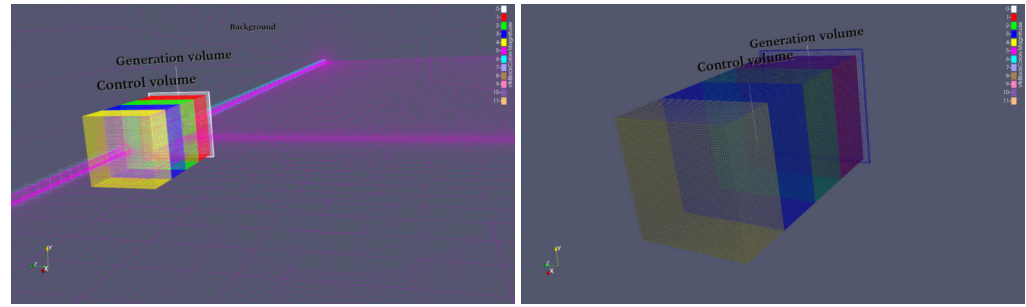

Figure 5. Layout of the computational domain grid (left) and details of the generation and control blocks (right) The control block is splitted into 4 sub-blocks.

A gradient pressure condition is imposed at the outlet section and velocity condition is enforced at the external boundary.

The numerical solution is performed by distributed and shared memory parallelization, by using the OpenMP API. In order to balance the load on all nodes, the control block is split in the streamwise direction into 4 sub-blocks with an equal number of cells, see Fig. 5. Using MPI, the solution on each split block is calculated as a separate process. Once the flow field solution is evaluated, the analysis of statistical properties of the turbulent flow is performed by rebuilding the solution into a single block.

In the present problem, no solid boundaries in the fluid domain exist. In such a condition, the DES model reduces to a LES throughout the computational domain. A time-marching solution for unsteady flows is evaluated. The simulation is initialised with a sudden start. At time $t = 0$, the volume force distribution in Eq. (17) is initialised with $k_i(0) = 10^{-5}$. At each time step, the intensity is updated by the PID control strategy in order to achieve imposed values of turbulence in the flow, as described in Section 3.2.

The residuals of velocity components and pressure for the solution on the finest grid level are shown in Fig. 6. The velocity components u_i converge to residual values in the order of 10^{-4} after more than 1000 iterations. Similarly acceptable value of CFL (Courant-Friedrichs-Lewy) below 1 are established.
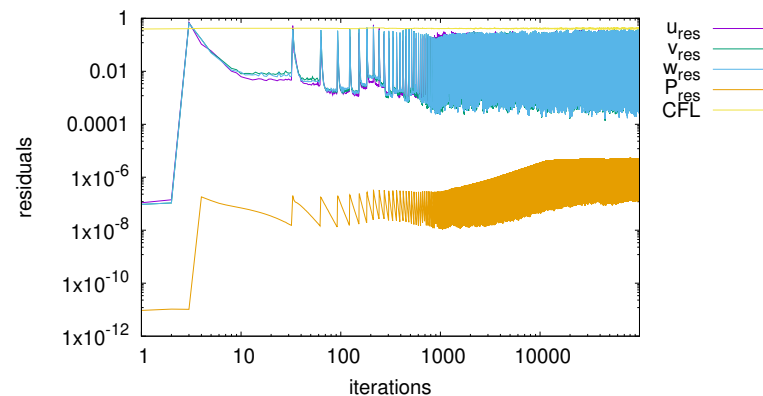

Figure 6. Residuals of velocity components and pressure, CFL condition.

5.2. Flow field simulations

The simulation described here deals with a uniform onset flow at $Re = 1.25 \cdot 10^6$. The objective is to generate a homogeneous and isotropic turbulent flow regime with 16% intensity ($I_{\infty,des} = 0.16$). The Reynolds number is evaluated as $Re = Lu_\infty/\nu$, where $L = 0.5$ m, $u_\infty = 2.5$ m/s and $\nu = 1.004 \cdot 10^{-6}$ m^2/s. The physical time step used for the time marching solution is $\Delta t = .001047$ s. Recalling the grid block dimensions in Table 1, about 780 time steps are required to cover at nominal flow speed u_∞ the distance between the

center of the generation block and the downstream end of the control block. The convection time from the generation block to the downstream end of the control block, $T_{conv} = 780\,\Delta t$, is taken as a reference to denote the duration of the initial transient-flow phase. This definition is consistent with the residuals plot in Fig. 17.

The results presented in this Section describe the flow field solution in the finest grid level. The development of turbulent flow as effect of the interaction between the onset uniform flow and the volume force distribution is illustrated in Fig. 7, where the streamwise component of the flow velocity, u_1, and of the vorticity magnitude $\zeta = \|\nabla \times \mathbf{u}\|$ are plotted. Both distributions describe the flow field at a representative time step following the initial transient-flow phase, at $t > T_{conv}$. The onset flow is directed left to right. The perturbation induced by the volume force distribution over a thin region normal to the x_1 direction is clearly visible on the left side of the computational domain. The sudden formation of eddies downstream of the generation volume is apparent, whereas outside the wake shed by the volume force region the flow remains unperturbed, except for a transition region where mixing between the turbulent stream and the unperturbed flow is observed. Similarly, snapshots of the velocity components u_2, u_3 at the same time step are presented in Fig. 8.
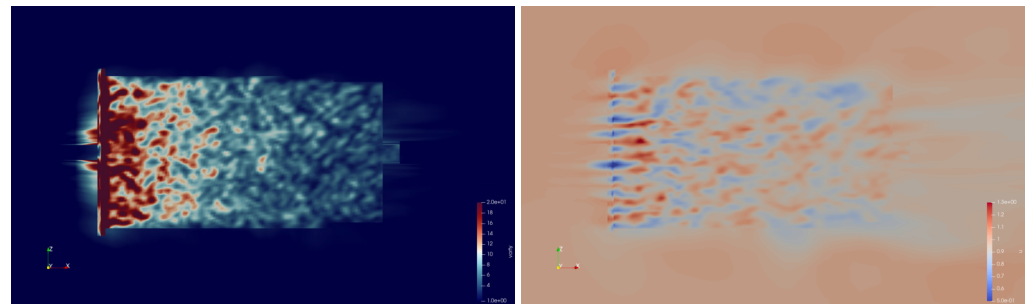

Figure 7. Effect of turbulence generation on the flow field downstream of the generation region. Left: turbulence intensity. Right: u_1 velocity component. Representative time step $t_1 > T_{conv}$.
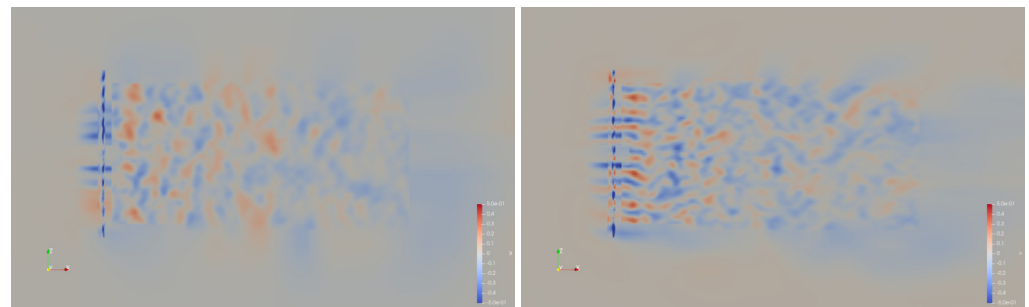

Figure 8. Flow velocity components u_2 (left) and u_3 (right) at representative time step $t_1 > T_{conv}$.

A three dimensional visualization of eddies describing the generated turbulent structures can be obtained by considering the eigenvalues of the tensor $\mathbf{A}^2 + \mathbf{\Omega}^2$, where $\mathbf{A}$ and $\mathbf{\Omega}$ represent, respectively, the symmetric and anti-symmetric parts of the velocity gradient tensor

$$\mathbf{A} = \frac{1}{2}\left(\nabla\mathbf{u} + \nabla\mathbf{u}^T\right), \qquad \mathbf{\Omega} = \frac{1}{2}\left(\nabla\mathbf{u} - \nabla\mathbf{u}^T\right). \tag{18}$$

By ordering the eigenvalues evaluated at each field point such that $\lambda_1 \geq \lambda_2 \geq \lambda_3$, vortex structures can be identified by connected regions where λ_2 is lower than a suitable negative value that depends on the flow conditions [34].

Figure 9 presents the λ_2 iso–surfaces at a representative time step, whereas the colormap on the surface denotes the vorticity magnitude ζ. For the sake of clarity, only a portion of the computational domain discretized by generation and control blocks is shown. The inner part of this region is made visible by removing the cells in a quarter of the control block as illustrated in left Fig. 9. The λ_2 plot reveals the random fluctuation of the turbulent

structures as effect of the mutual interaction among eddies. The diffusion and dissipation of structures as the distance from the generation area increases is witnessed by the vorticity intensity levels associated to the turbulent structures.
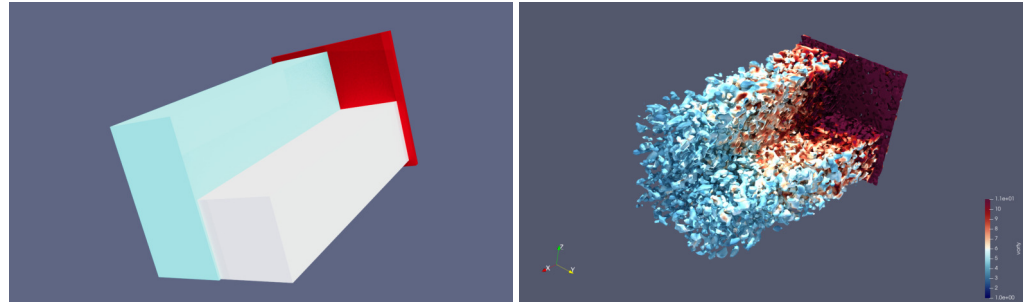

Figure 9. Iso–surfaces of the λ_2 quantity and colormaps of the vorticity magnitude on the generation block and on a portion of the control block (right). Sketch of the considered control block portion (left).

The visualization of flow variables like velocity, vorticity or derived quantities like the λ_2 parameter, provide only a qualitative insight to the generated turbulent flow. Further analysis is necessary to determine key turbulent metrics quantities, and to verify the stationarity of the solution at time $t > T_{conv}$. In particular, the possibility that homogeneous, isotropic turbulence conditions are established with desired turbulence intensity levels is to be investigated.

To this aim, spatial mean values $\overline{u_i}$ and variance σ_i^2 of the velocity components u_i have been evaluated in the flow region occupied by the control block, see right Fig. 5.

In particular, the spatial mean reads

$$\overline{u_i}(\mathbf{x}, t) = \frac{1}{V} \int_V u_i(\boldsymbol{\xi} + \mathbf{x}, t) d\boldsymbol{\xi} \qquad (i = 1, 2, 3) \tag{19}$$

The quantities are evaluated at each time step and further averaged over time steps t_k such that $t_k > T_{conv}$. The symbol $< \ >$ is used to denote the aritmetic mean on all samples at time steps t_k. The results are presented in Table 2, where the averaged mean velocity terms $< \overline{u_i} >$ are normalized with respect to the nominal flow speed u_∞.

In order to capture the variability of the flow metrics as the distance from the generation region increases, quantities $< \overline{u_i} >$ and $< \sigma_i^2 >$ evaluated on the whole control block are compared with the corresponding values obtained for each of the four sub-blocks in which the main block is split, as shown in right Fig. 5. Specifically, the sub-blocks have identical dimensions and discretization and are numbered 1 to 4 in the streamwise direction. Each block centre is labelled as point P_i, with i from 1 to 4, see Fig. 10.
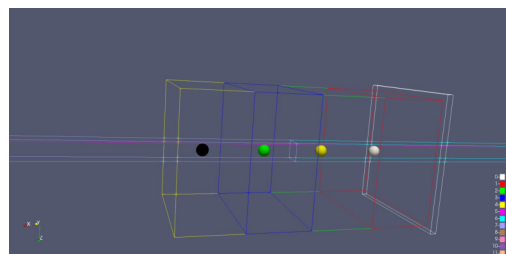

Figure 10. Control block split into 4 sub-blocks in the streamwise direction. Sub-block centers denoted as points P_i with i from 1 to 4.

From Table 2, a first important result is that the mean velocity in the streamwise direction is lower than the unperturbed flow velocity, with $< \overline{u_i} > / u_\infty = 0.933$ in the whole control block. The observed 6.67% velocity defect can be explained with the blockage

Table 2. Averaged mean value $< \overline{u_i} >$ and variance $< \sigma_i^2(\overline{u_i}) >$ of the velocity components $u_i(i = 1, 2, 3)$ in the control block and in the 4 sub-blocks.

		$i = 1$	$i = 2$	$i = 3$
Control block	$< \overline{u_i} > /u_\infty$	0.933	-0.0356	-0.0378
	$< \sigma_i^2(\overline{u_i}) >$	$0.788 \ 10^{-2}$	$0.686 \ 10^{-2}$	$0.681 \ 10^{-2}$
Sub block 1	$< \overline{u_i} > /u_\infty$	0.931	-0.0456	-0.0478
	$< \sigma_i^2(\overline{u_i}) >$	$0.174 \ 10^{-1}$	$0.146 \ 10^{-1}$	$0.146 \ 10^{-1}$
Sub block 2	$< \overline{u_i} > /u_\infty$	0.931	-0.0359	-0.0379
	$< \sigma_i^2(\overline{u_i}) >$	$0.696 \ 10^{-2}$	$0.602 \ 10^{-2}$	$0.599 \ 10^{-2}$
Sub block 3	$< \overline{u_i} > /u_\infty$	0.935	-0.0318	-0.0339
	$< \sigma_i^2(\overline{u_i}) >$	$0.387 \ 10^{-2}$	$0.347 \ 10^{-2}$	$0.342 \ 10^{-2}$
Sub block 4	$< \overline{u_i} > /u_\infty$	0.938	-0.0290	-0.0315
	$< \sigma_i^2(\overline{u_i}) >$	$0.250 \ 10^{-2}$	$0.228 \ 10^{-2}$	$0.225 \ 10^{-2}$

due to the volume force distribution used to generate turbulent eddies. This phenomenon is well known with physical grids that are used in laboratories to stimulate turbulence.

The volume force distribution also determines a deviation of the unperturbed onset flow, with normalised mean values $< \overline{u_2} > /u_\infty = -0.0356, < \overline{u_3} > /u_\infty = -0.0378$ of the velocity components normal to the nominal streamwise direction x_1. Such a flow distortion can be explained with non zero resultants of the randomly generated volume force terms in the x_2, x_3 directions.

If mean velocity values from the sub-blocks are considered, it can be noted that the velocity defect in the streamwise direction tends to reduce as the distance from the generation block increases, as effect of diffusion of the wake downstream of the generation block. In particular, $< \overline{u_1} > /u_\infty$ increases from 0.931 in sub-block 1 to 0.938 in sub-block 4. Stronger reductions of mean values $< \overline{u_2} >$ and $< \overline{u_3} >$ are observed, with the result that the above mentioned distortion of the flow is partially recovered.

Results in Table 2 for the variance $< \sigma_i^2 >$ highlight a significant dissipation of turbulent structures in a narrow region downstream of the generation block. In the nominal streamwise direction, one has $< \sigma_1^2 >= 0.0174$ in the first sub-block and $< \sigma_1^2 >= 0.0025$ in the fourth sub-block, whereas the average across the four sub-blocks is 0.0079. In all sub-blocks, the variance in the x_2, x_3 directions are almost identical and slightly lower than the variance in the streamwise direction.

The variance values $< \sigma_i^2 >$ evaluated on the whole control block, correspond to a turbulence intensity $I_\infty = 0.1589$ by using the definition in Eq. 13. This value is in good agreement with the desired value $I_{\infty,des} = 0.16$ and is the result of the PID control strategy described in Section 3.2. However, it should be noted that the quantities $< \sigma_i^2 >$ observed by the controller are evaluated in the sub-block 1 which is the closest one to the generation block. Recalling the dissipative trend observed by comparing results from the four sub-blocks, it can be expected that the turbulence intensity decreases moving from sub-block 1 to 4. In fact, the value obtained at the sub-block 1 is about 30% higher than the $I_\infty = 0.1589$ average over the four sub-blocks.

The role played by the PID controller in the achievement of a given turbulence intensity value is analysed in Fig. 11, where the errors $\mathcal{E}_i$ evaluated by Eq. 15 and referred to the three velocity components, are plotted as a function of the time step. The results highlight that the PID errors do not reduce to 0 with the iterations. After few time steps, $\mathcal{E}_1$ drops to about 0.25, and 0.35 for the other two components. However, these quantities do not reduce further during the iterative solution and oscillate about the above mentioned values. This trend is consistent with the discrepancy between expected and evaluated turbulence intensity observed above.

Once the time-marching solution reaches the fully developed turbulent flow condition, the stationarity of flow properties should be achieved. However, as shown in Fig. 11, the PID control used to match an imposed turbulence intensity value introduces some
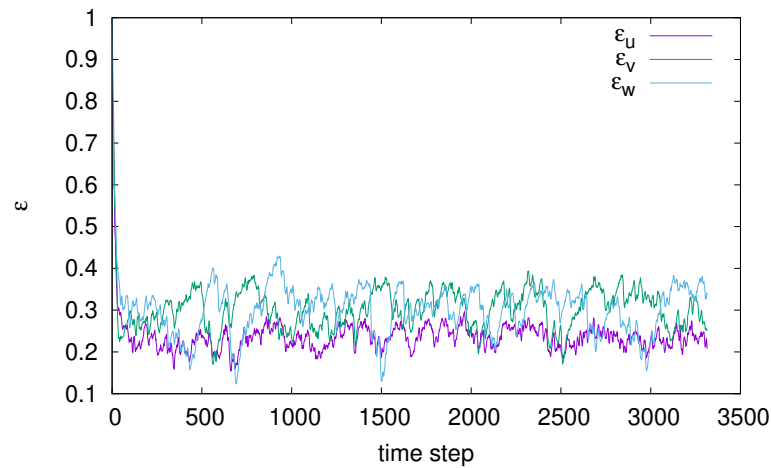
Figure 11. PID control error for the three velocity components as a function of time.

fluctuations in the intensity of the volume force terms that do not extinguish with time. Hence, the capability of the turbulent solution to achieve a stationary condition is a key aspect to be investigated. To this purpose, the evolution in time of flow field quantities at selected points is analyzed by considering the points P_1 to P_4 positioned in the center of each of the 4 sub-blocks, see Fig. 10. The streamwise distance of points P_1 to P_4 from the center of the generation block is, respectively, $0.275L, 0.775L, 1.275L, 1.775L$. These points are taken as virtual probes in the computational domain and the time series of fluctuating velocity components observed at those locations are processed to determine correlations, Fourier transforms, Power Spectral Density (PSD), Probability Density Functions (PDF).

First, the flow is analyzed by considering the evolution in time of the time average of velocity components referred to a time bin T_A assumed to be small as compared to the full computational time. For example, by averaging the streawise velocity component u_1, this yields

$$\tilde{u}_1(\mathbf{x}, t) = \frac{1}{T_A} \int_{-T_A/2}^{T_A/2} u_1(\mathbf{x}, t + \tau) d\tau \tag{20}$$

with arbitrary $t > T_A/2$. The symbol $(\tilde{\ })$ is used here to distinguish time-bin averaging from standard average evaluated on the full set of time samples $t_k < T_{conv}$, denoted by the symbol $< \ >$ and used in Table 2 above.

Figure 12 shows the time-bin averages evaluated by Eq. (20) for the three velocity components, as the central step t of the time bin increases. In the present analysis, the time-bin interval T_A has been taken equal to 500 time steps.

For comparison, the actual velocity values at each time step are also shown. The results relative to probe no. 4 demonstrate that in spite of the strong random fluctuations of the velocity, and of the oscillations of the volume force intensity induced by the PID controller, the time bin averaged values are almost constant throughout the considered time period.

Mean values and variance evaluated from time series of velocity components at the four probes P_i and $t > T_{conv}$ are presented in Table 3.

The above results by time averaging data from a single probe confirm the key trends observed from spatial averaging on each sub-block in Table 2. A non negligible velocity defect in the streamwise direction, and a significant reduction of variance terms σ_i^2 as the distance from the turbulence generation region increases are found in Table 3. A quantitative comparison among results from the two tables is presented in Fig. 13. Specifically, mean velocity terms $\overline{u_i}$ are compared in the top line plots. A significant discrepancy is observed between spatial averages on sub-blocks and corresponding quantities from probe signals at each sub-block center. The differences tend to rapidly reduce from sub-block 1 to
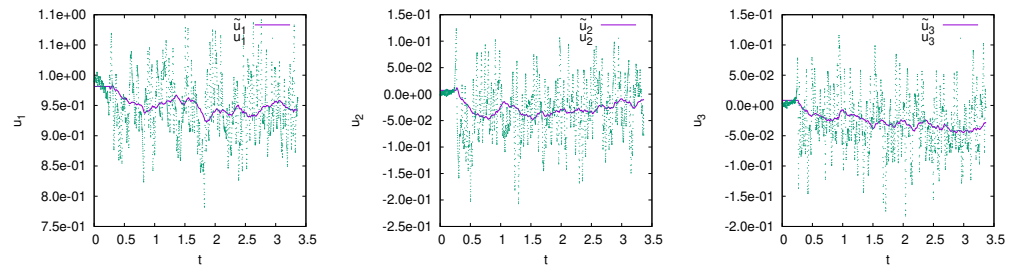
Figure 12. Probe no. 4: time series and time-bin average of the velocity components u_1 (left), u_2 (center), u_3 (right), evaluated by Eq. (20).

Table 3. Mean value $< \tilde{u}_i >$ and variance $< \sigma^2(\tilde{u}_i) >$ of velocity components $u_i (i = 1, 2, 3)$ from time series at probes P_j ($j = 1$ to 4) and $t > T_{conv}$.

		$i = 1$	$i = 2$	$i = 3$
Probe P_1	$< \tilde{u}_i > / u_\infty$	0.986	-0.041	-0.020
	$< \sigma^2(\tilde{u}_i) >$	$0.193\ 10^{-2}$	$0.156\ 10^{-2}$	$0.156\ 10^{-2}$
Probe P_2	$< \tilde{u}_i > / u_\infty$	0.956	-0.029	-0.031
	$< \sigma^2(\tilde{u}_i) >$	$0.810\ 10^{-2}$	$0.672\ 10^{-2}$	$0.792\ 10^{-2}$
Probe P_3	$< \tilde{u}_i > / u_\infty$	0.952	-0.028	-0.027
	$< \sigma^2(\tilde{u}_i) >$	$0.410\ 10^{-2}$	$0.360\ 10^{-2}$	$0.372\ 10^{-2}$
Probe P_4	$< \tilde{u}_i > / u_\infty$	0.949	-0.027	-0.027
	$< \sigma^2(\tilde{u}_i) >$	$0.260\ 10^{-2}$	$0.292\ 10^{-2}$	$0.221\ 10^{-2}$

sub-block 4, that is, moving downstream of the turbulence generation region. This trend is common to all the velocity components. Considering variance terms σ_i^2, bottom line plots in Fig. 13, the differences between the two datasets are small on the upstream blocks and tend to vanish moving further downstream. These results demonstrate that the generated turbulent flow field tends to spatial homogeneity at some distance downstream of the generation region, and as the solution evolves, stationarity of mean velocity components is also established with a good approximation. Except for a narrow region in proximity of the turbulence generation block, a good agreement between spatial and time averages is found. It may be concluded that the generated turbulent field has an acceptable level of ergodicity.
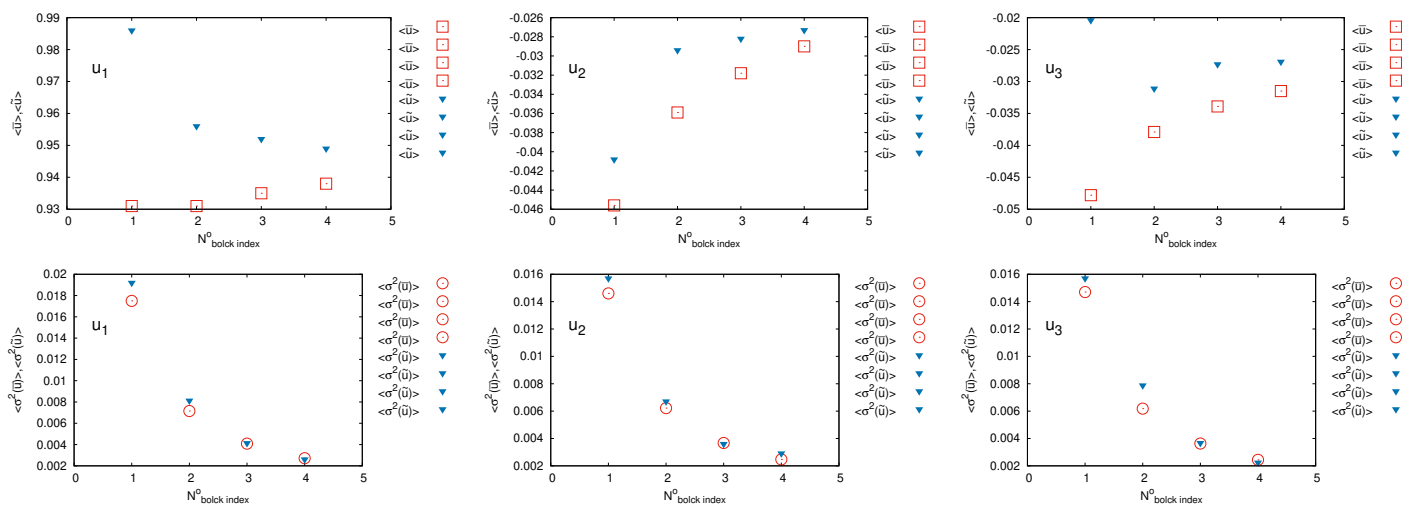

Figure 13. Comparison of mean velocity $\overline{u_i}$ and variance σ_i^2 for all velocity components by spatial averaging on sub-blocks 1 to 4 and by time averaging at probes P_1 to P_4.

For the sake of completeness, time series of the standard deviation of each flow velocity component are presented in Fig. 14. Specifically, time-bin averaged data from single probes at sub-block centers and spatially averaged data over each sub-block are compared.
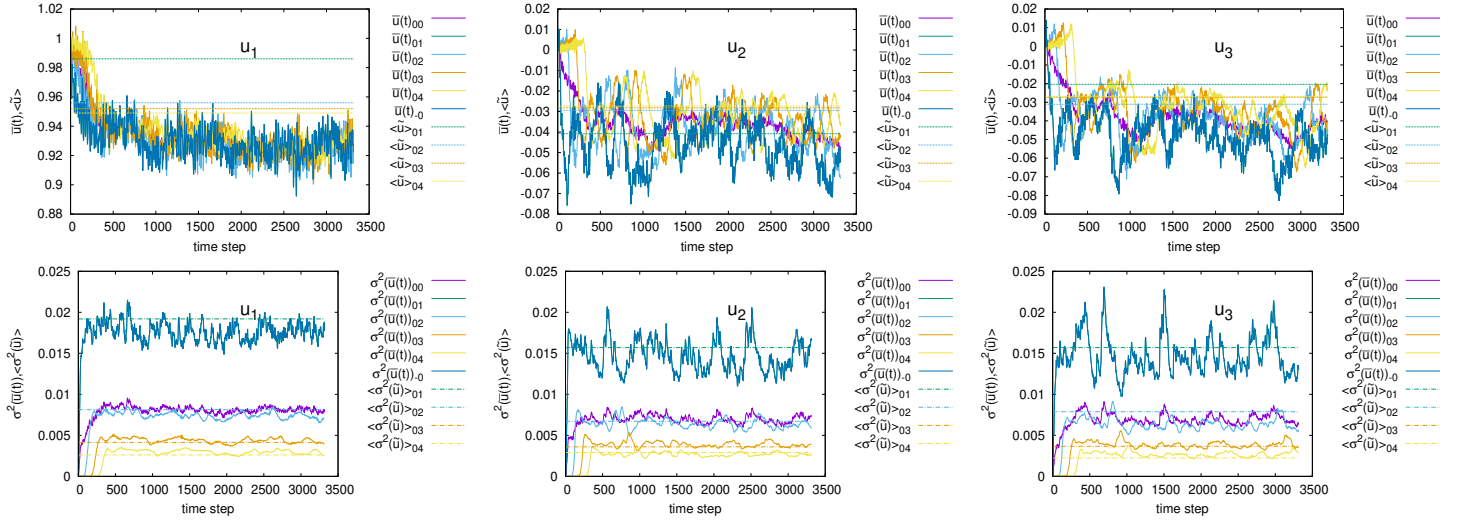

Figure 14. Standard deviation of velocity components from time-bin averaging at sub-block probes and from spatial averaging over sub-blocks. Top: $\overline{u}(t), <\tilde{u}>$; bottom: $\sigma^2(\overline{u}(t)), <\sigma^2(\tilde{u})>$. Left to right: velocity components u_1, u_2, u_3.

Figure 15 presents the time auto-correlation $R_{ii}(\tau)$ defined in Section 3.1, applied here to the three velocity components at probe P_4. As expected, the correlation rapidly drops to very small values as the correlation time increases. From these diagrams, the integral time scale $\mathbb{T}$ can be evaluated as

$$\mathbb{T} = \frac{1}{R_{ii}(0)} \int_0^\infty R_{ii}(\tau)d\tau \qquad (i = 1, 2, 3) \tag{21}$$

Considering as example the probe P_1, the following values are obtained: $\mathbb{T}_{u_1} = 7.06\,10^{-3}, \mathbb{T}_{u_2} = 1.3\,10^{-3}, \mathbb{T}_{u_3} = 2.98\,10^{-3}$.
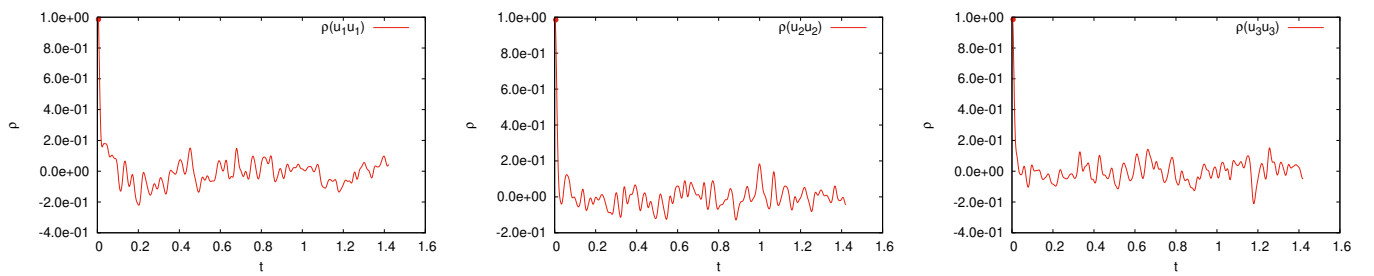

Figure 15. Probe no. 4: time auto-correlation $R_{ii}(\tau)$ of the velocity components u_1 (left), u_2 (center), u_3 (right).

The Power Spectral Density (PSD) of the kinetic energy is evaluated as

$$S(f) = \frac{1}{\sqrt{2\pi}} \sum_{n \in \mathbb{Z}} e^{-i2\pi f n} R(n), \quad f \in [0, 1] \tag{22}$$

where $R(n) = E[X_n X_0]$ is the autocorrelation function of a stationary random process X_n and $n \in \mathbb{Z}$ is an arbitrary integer number.

Figure 16 presents the PSD calculated at probes P_i. In the non–inertial range, a relatively good agreement with Kolmogorov's -5/3 law is observed, with the exception of probe no. 4 (bottom right plot).
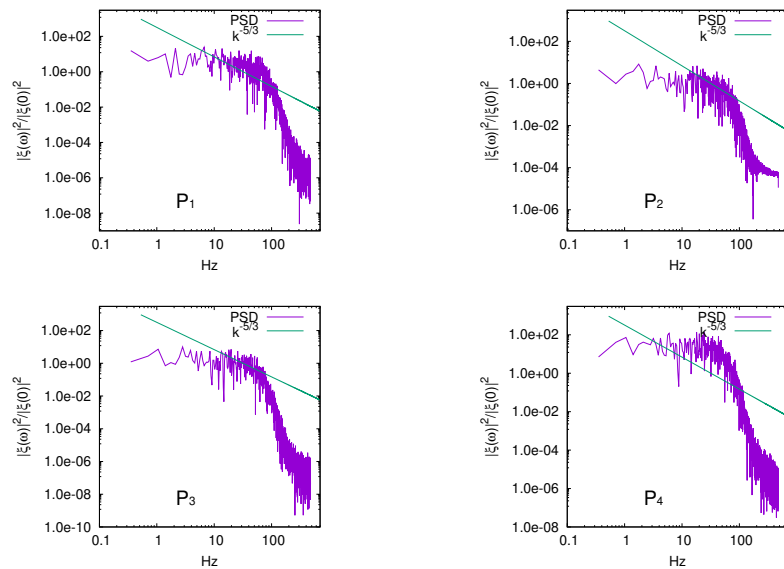
Figure 16. Kinetic energy Power Spectral Density (PSD) at probes P_i with $i = 1$ to 4, left to right, top to bottom.

In order to estimate the anisotropy of the turbulent flow, the analysis of the correlation tensor as proposed in [36], is performed. Figure 17 depicts the position of velocity component pairs (u_1, u_2) (left) and (u_1, u_3) (right) in the corresponding (u_1, u_2) and (u_1, u_3) planes. The results are referred to velocity samples from each cell in the control block. With few exceptions, all pairs fall within a circle centered in the origin. This provides a qualitative estimate of the isotropy of the generated flow field. A relative eccentricity of pairs towards negative u_2 and u_3 values is observed, as already noted by flow visualizations in Fig. 8.
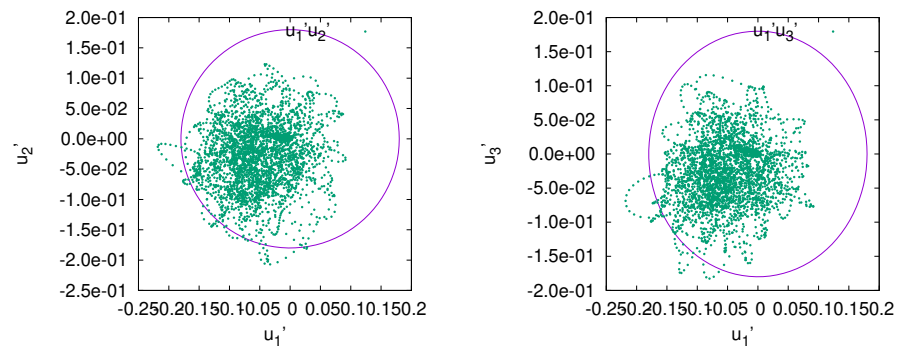

Figure 17. Correlation maps between velocity component pairs (u_1, u_2) (left) and (u_1, u_3) (right).

Following [33] and [37], further information can be obtained from the invariants of the tensor **S** defines as $S_{ij} = R_{ij}(0) - 1/3 R_{ii}(0)\delta_{ij}$.

To this purpose, the first three tensor invariants are considered

$$\mathbb{I} = S_{ii}; \qquad \mathbb{II} = \frac{1}{2}[(S_{ii})^2 - S_{ii}^2]; \qquad \mathbb{III} = det(\mathbf{S}), \qquad (23)$$

In particular, the isotropy of a random signal can be investigated by mapping events in the $(\mathbb{II}, \mathbb{III})$ plane. Two lines departing from the origin $(0,0)$ delimit the region where invariant pairs $(\mathbb{II}, \mathbb{III})$ for a random signal are expected. A perfectly isotropic signal is characterized by invariant values $\mathbb{II} = 0$ and $\mathbb{III} = 0$. Figure 18 presents the results for the generated turbulent flow. Specifically, the events corresponding to 20 representative time steps at the 4 virtual probes P_i are considered in separate diagrams. All events are within the feasible

region, and points tend to cluster close to the origin as the distance of the probe from the generation region increases (top to bottom, left to right in the figure). The results highlight that at some distance downstream from the generation region, the generated turbulent structures evolve into a nearly isotropic flow.
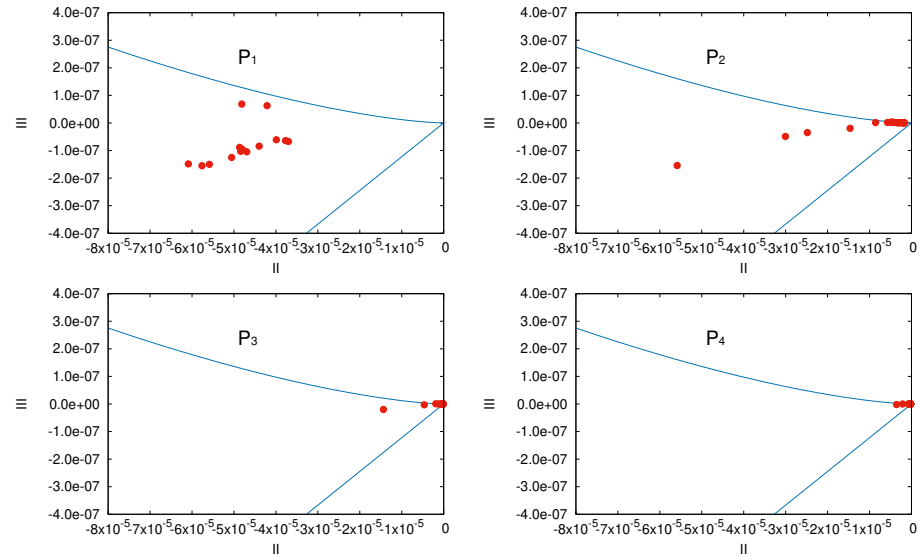

Figure 18. Isotropy diagrams by using S_{ij} tensor invariants (II, III) from Eq. 23. Top to bottom, left to right: Probe 1 to 4.

Further insight to the isotropy in the established turbulent flow can be obtained by evaluating the Probability Density Function (PDF) of the velocity components at the four probes P_i and comparing with a normal Gaussian distribution. The results are shown in Fig. 19 for the three velocity components and all probes P_i, with $i = 1$ to 4. The probes PDFs are compared with Gaussian distributions with same mean values and variance as the calculated velocity components, as described in Tables 2 and 3 above. With some approximation, the evaluated PDFs for all combinations of probe and velocity component fairly match the corresponding Gaussian distributions. Some deviations with significant skewness and kurtosis are found in the distributions for cases $u_1(P_1)$ and $u_1(P_2)$ (respectively, first and second line from top, left column), $u_2(P_1)$, $u_2(P_3)$ and $u_2(P_4)$ (respectively, first, third and forth line from top, center column), and $u_3(P_2)$, $u_3(P_3)$ (respectively, second and third line from top, right column). It can be noted that the deviations from the expected Gaussian distribution do not present a clear trend with the position of the considered probe.

5.3. Discussion

The methodology outlined in Section 3 provides a simple formulation to generate a random perturbation to simulate onset turbulence in the numerical solution by CFD of an arbitrary viscous flow. The perturbation originates by an obstacle to the unperturbed flow that is modelled as a distribution of volume forces. A direct analogy is found with physical grids used in the experimental field to generate turbulent flows in tunnel test sections. The modelling of a physical grid as a volume force distribution is computationally quite efficient as compared with the representation of physical grid elements as solid boundaries in the computational domain. In addition to that, the volume force distribution can be dynamically adjusted to modify the flow field perturbation that is generated. In the present approach, a full variability of the perturbation is obtained by a volume force distribution that is randomly variable in time and space and whose intensity can be further scaled through a dedicated control strategy.

The numerical application illustrated in Section 5 has been performed with the objective to investigate if such a simple and computationally efficient model can generate flow field perturbations that are representative of real turbulent flows. In spite of its extreme
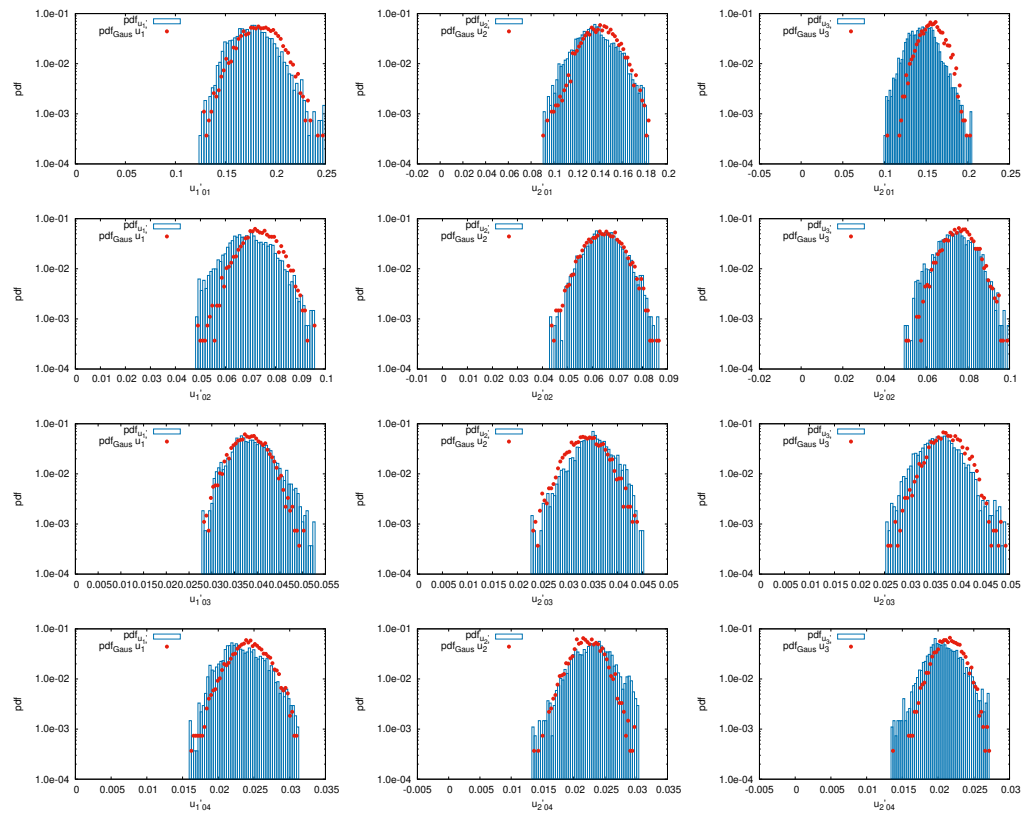
Figure 19. Probability Density Function (PDF) of velocity components u_1 (left), u_2 (center), and u_3 (right) compared with normal Gaussian distributions. Top to bottom: probes P_i, with i from 1 to 4.

simplicity, the proposed numerical application provides an appealing case study. The methodology implies that a grid block is dedicated to the volume force distribution. The turbulent structures generated within this block are shed downstream in a flow region that gradually expands in the direction normal to the streamwise direction as effect of the diffusion of turbulent eddies. The utilization of a control strategy to adjust the intensity of volume force terms to target flow conditions, implies that relevant statistical flow properties are evaluated at virtual probes and over control volumes in suitable positions in the computational domain. In the present numerical application, a grid block covering a wide portion of the field downstream of the generation area has been considered to collect data for the control algorithm, Fig. 5. In general, the use of a dedicated control block is not necessary. Nevertheless, the time stepping of the solution and the spatial discretization of the domain portion used to collect control strategy input data should be adequate for the correct evaluation of statistical properties as mean, variance and correlation of velocity components, power spectral density, probability density functions. In particular, time stepping and grid refinement are responsible for the length and time scales of the turbulent structures that can be modelled. A simple elaboration of data in Table 1 shows that in the present study, eddies with size larger than approximately $0.02L$ can be described, assuming that at least a 2×2 cells square stencil is necessary to detect a planar eddy.

The results of flow field simulations highlight that the perturbation induced by the volume force distribution is characterized by a rapid evolution downstream of the generation region. The dynamics of the turbulent structures is governed by the model used for the numerical solution of the viscous turbulent flow, as shown in Figs. 7 to 9. A DES model has been considered in the present study. At some distance downstream of the turbulence generation area, the flow tends to achieve satisfactory levels of stationarity. Small fluctuations of the velocity components are largely due to time variations of the volume force intensity caused by the PID controller that is not able to reduce to zero the

control error (Fig. 11). In the downstream region, the flow tends to be ergodic as shown by the good agreement between time averages and spatial averages of the mean velocity and variance, as demonstrated in Fig. 13. Similarly, flow anisotropy observed close to the generation region is rapidly reduced moving downstream, Fig. 18.

For the particular case considered in the present analysis, it may be concluded that at some distance downstream of the generation region, a fully developed turbulent flow with satisfactory stationarity and isotropy characteristics is established. The quantitative comparison between requested and obtained mean flow velocity and turbulence intensity can be also positively evaluated. As expected, a 6-7% velocity defect is observed downstream of the region where volume force terms are imposed, whereas the unperturbed mean flow velocity is partially recovered as the distance from the generation area increases. The turbulence intensity evaluated by averaging over a large portion of the flow fairly matches the requested value, with evaluated $I_\infty = 0.159$ against a desired value of 0.16. However, a rapid decay of turbulence intensity has been observed in a narrow region downstream of the generation area. Both mean flow velocity and turbulence intensity tend to reach uniform values at larger distance downstream. An advanced control strategy can be used to ensure that values close to the expected ones are achieved at some distance downstream of the generation area. The results obtained in the present study provide only an initial verification of the proposed methodology. The capability to generate turbulent flows with different intensity levels and the application to complex configurations with solid bodies immersed into the flow has to be demonstrated. Similarly, the analysis of grid refinement on the properties of the generated turbulence is also necessary.

6. Conclusions

A theoretical and computational methodology for the generation of onset turbulent flows with prescribed properties in the numerical simulation of an arbitrary viscous flow has been presented. The proposed technique falls within the class of synthetic volume force methods, in which turbulent eddies are generated by a suitable distribution of volume force terms in the right–hand side of the Navier–Stokes equations. In the present formulation, the distribution is defined as a combination of harmonic functions that are randomly variable in time and space. A control strategy is used to enforce that the generated turbulent structures match an imposed turbulence intensity level and a homogeneous isotropic flow is established. Although the approach is general, the proposed methodology is primarily intended for the computational modelling of hydrokinetic turbines in a turbulent onset flow representative of tidal or riverine installations.

A first numerical application has been presented by considering the injection of homogeneous and isotropic turbulence with 16% intensity into a uniform unbounded flow. Flow field calculations have been performed by Detached Eddy Simulation, by using a computational set-up valid for the analysis of model-scale tidal turbine performance in a real onset turbulent flow. The resulting flow field has been analysed in terms of flow statistical properties as auto-correlation, power spectral density, probability density functions. The results demonstrate that at small distance downstream of the turbulence generation area, the flow tends to achieve satisfactory levels of stationarity and isotropy. A small velocity defect is observed downstream of the turbulence generation region, whereas the unperturbed mean flow velocity is partially recovered as the distance increases. The mean turbulence intensity evaluated over a large portion of the flow fairly matches the requested value. However, a significant decay of turbulence intensity has been observed at increasing distance downstream of the generation area.

From this notional numerical application it can be concluded that the proposed methodology represents a promising approach to simulate onset turbulent flow conditions. Established flow properties are consistent with the computational analysis of hydrokinetic turbines operating in tidal and riverine sites. Significant improvements of present results are expected by introducing advanced volume force control strategies to replace the simple PID controlled used in these preliminary calculations. The application of the proposed

methodology to the computational analysis of single turbines and arrays of turbines is the subject of ongoing work.

Author Contributions: Conceptualization and methodology, M.G. and F.S; software and validation, M.G.; formal analysis and investigation, M.G, F.S., R.M.; writing—original draft preparation, M.G, F.S.; writing—review and editing, F.S, R.C.; funding acquisition, F.S. All authors have read and agreed to the published version of the manuscript.

Conflicts of Interest: The authors do not declare conflicts of interest.

Abbreviations

The following abbreviations are used in the manuscript:

CFL	Courant-Friedrichs-Lewy
DES	Detached eddy simulation
DNS	Direct numerical simulation
LES	Large eddy simulation
N-S	Navier-Stokes Equation
PM	Precursor Methods
PID	Proportional Integral Derivative
PSD	Power Spectral Density
PDF	Probability Density Function
SM	Synthetic Method
SDFM	Synthetic Digital Filtering Method
SVFM	Synthetic Volume forcing Metho
SRFM	Synthetic Random Fourier Method

Appendix A Summary of statistical relationships

The analysis of turbulent flows involves the evaluation of statistical functions that are used to determine quantitative information through an adequate metrics. For the sake of completeness, a brief summary of main statistical relationships used in the paper is given here, whereas a comprehensive formulation can be found, *e.g.*, in [38].

The statistical analysis of interest here grounds on the so–called Reynolds decomposition of an arbitrary fluid-dynamics variable X as a mean value and its fluctuation,

$$X = E[X] + X' \tag{A1}$$

where $E[X]$ denotes the *expected value* of X

$$E[X] = \int_{-\infty}^{+\infty} x\, f_X(x)\, dx \tag{A2}$$

whereas X' is the fluctuation. In Eq. (A2), the function $f_X(x)$ represents the probability density function of the events associated to the variable X. By definition, the fluctuation has a zero mean value, or $E[X'] = 0$.

By introducing $\mu = E[X]$, and recalling $E[\ ]$ is a linear operator, the following relationships for the *variance* σ^2 hold

$$\sigma^2(X) = E[(X - \mu)^2] = E[X^2] - \mu^2 \tag{A3}$$

and hence $\sigma^2(X) = E[X^2]$, for the particular case of zero–mean signals.

References

1. Pecoraro, A.; Felice, F.D.; Felli, M.; Salvatore, F.; Viviani, M. An improved wake description by higher order velocity statistical moments for single screw vessel. *Ocean Engineering* **2015**, *108*, 181–190. doi:https://doi.org/10.1016/j.oceaneng.2015.07.038.

2. Gant, S.; Stallard, T. Modelling a Tidal Turbine in Unsteady Flow. *Proceedings of the International Offshore and Polar Engineering Conference* **2008**.

3. Allmark, M.; Martinez, R.; Ordonez-Sanchez, S.; Lloyd, C.; O'Doherty, T.; Germain, G.; Gaurier, B.; Johnstone, C. A Phenomenological Study of Lab-Scale Tidal Turbine Loading under Combined Irregular Wave and Shear Flow Conditions. *Journal of Marine Science and Engineering* **2021**, *9*. doi:10.3390/jmse9060593.

4. Togneri, M.; Pinon, G.; Carlier, C.; Choma Bex, C.; Masters, I. Comparison of synthetic turbulence approaches for blade element momentum theory prediction of tidal turbine performance and loads. *Renewable Energy* **2020**, *145*, 408–418. doi:10.1016/j.renene.2019.05.110.

5. Allmark, M.; Ellis, R.; Ebdon, T.; Lloyd, C.; Ordonez-Sanchez, S.; Martinez, R.; Mason-Jones, A.; Johnstone, C.; O'Doherty, T. A detailed study of tidal turbine power production and dynamic loading under grid generated turbulence and turbine wake operation. *Renewable Energy* **2021**, *169*, 1422–1439. doi:https://doi.org/10.1016/j.renene.2020.12.052.

6. Sentchev, A.; Thiébaut, M.; Schmitt, F.G. Impact of turbulence on power production by a free-stream tidal turbine in real sea conditions. *Renewable Energy* **2020**, *147*, 1932–1940. doi:https://doi.org/10.1016/j.renene.2019.09.136.

7. Mycek, P.; Gaurier, B.; Germain, G.; Pinon, G.; Rivoalen, E. Experimental study of the turbulence intensity effects on marine current turbines behaviour. Part II: two interacting turbines. *Renewable Energy* **2014**, *68*, 876–8892. doi:https://doi.org/10.1016/j.renene.2013.12.036.

8. Sellar, B.G.; Wakelam, G.; Sutherland, D.R.J.; Ingram, D.M.; Venugopal, V. Characterisation of Tidal Flows at the European Marine Energy Centre in the Absence of Ocean Waves. *Energies* **2018**, *11*. doi:10.3390/en11010176.

9. Sentchev, A.; Thiébaut, M.; Sylvain, G., Turbulence characterization at tidal-stream energy site in Alderney Race; 2020; pp. 616–623. doi:10.1201/9781003134572-70.

10. Tabor, G.; Baba-Ahmadi, M. Inlet conditions for large eddy simulation: A review. *Computers and Fluids* **2010**, *39*, 553–567. doi:https://doi.org/10.1016/j.compfluid.2009.10.007.

11. R, C.D.F.D.G.M. A Generalised Unsteady Hybrid RANSE/BEM Methodology Applied to Propeller-Rudder Flow Simulation. *Seventh International Conference on Computational Methods in Marine Engineering (MARINE 2017)* **2017**.

12. Z., S.F.C.D.S. Development of a Viscous/Inviscid Hydrodynamics Model for Single Turbines and Arrays. *Twelwth European Wave and Tidal Energy Conference,EWTEC 2017* **2017**.

13. Gregori, M.; Calcagni, D.; Salvatore, F.; Di Felice, F.; Pereira, F.J.A.; Camussi, R., Hybrid viscous/inviscid modelling of a hydrokinetic turbine performance and wake field; 2020; pp. 553–562. doi:10.1201/9781003134572-63.

14. Muscari, R.; Di Mascio, A.; Verzicco, R. Modeling of vortex dynamics in the wake of a marine propeller. *Computers & Fluids* **2013**, *73*, 65–79. doi:https://doi.org/10.1016/j.compfluid.2012.12.003.

15. NA, Y.; MOIN, P. Direct numerical simulation of a separated turbulent boundary layer. *Journal of Fluid Mechanics* **1998**, *374*, 379–405. doi:10.1017/S002211209800189X.

16. Wu, X.; Squires, K.D.; Lund, T.S. Large Eddy Simulation of a Spatially-Developing Boundary Layer. Proceedings of the 1995 ACM/IEEE Conference on Supercomputing; Association for Computing Machinery: New York, NY, USA, 1995; Supercomputing '95, p. 67–es. doi:10.1145/224170.224408.

17. Zhu, W.L.; Yang, Q.S.; Cao, S.Y. Applicability research on the turbulent inflow for building les simulation. *Kongqi Donglixue Xuebao/Acta Aerodynamica Sinica* **2011**, *29*, 124–128.

18. Rogallo, R.S.; Moin, P. Numerical Simulation of Turbulent Flows. *Annual Review of Fluid Mechanics* **1984**, *16*, 99–137, [https://doi.org/10.1146/annurev.fl.16.010184.000531]. doi:10.1146/annurev.fl.16.010184.000531.

19. Adler, M.C.; Gonzalez, D.R.; Stack, C.M.; Gaitonde, D.V. Synthetic generation of equilibrium boundary layer turbulence from modeled statistics. *Computers & Fluids* **2018**, *165*, 127–143. doi:https://doi.org/10.1016/j.compfluid.2018.01.003.

20. di Mare, L.; Klein, M.; Jones, W.P.; Janicka, J. Synthetic turbulence inflow conditions for large-eddy simulation. *Physics of Fluids* **2006**, *18*, 025107, [https://doi.org/10.1063/1.2130744]. doi:10.1063/1.2130744.

21. Kraichnan, R.H. Diffusion by a Random Velocity Field. *The Physics of Fluids* **1970**, *13*, 22–31, [https://aip.scitation.org/doi/pdf/10.1063/1.16]. doi:10.1063/1.1692799.

22. Wu, X. Inflow Turbulence Generation Methods. *Annual Review of Fluid Mechanics* **2017**, *49*, 23–49, [https://doi.org/10.1146/annurev-fluid-010816-060322]. doi:10.1146/annurev-fluid-010816-060322.

23. Lee, S.; Lele, S.K.; Moin, P. Simulation of spatially evolving turbulence and the applicability of Taylor's hypothesis in compressible flow. *Physics of Fluids A: Fluid Dynamics* **1992**, *4*, 1521–1530, [https://doi.org/10.1063/1.858425]. doi:10.1063/1.858425.

24. Choma Bex, C.; Carlier, C.; Fur, A.; Pinon, G.; Germain, G.; Élie Rivoalen. A stochastic method to account for the ambient turbulence in Lagrangian Vortex computations. *Applied Mathematical Modelling* **2020**, *88*, 38–54. doi:https://doi.org/10.1016/j.apm.2020.05.035.

25. Rijpkema, D.; Starke, B.; Bosschers, J. Numerical simulation of propeller-hull interaction and determination of the effective wake field using a hybrid RANS-BEM approach. 2013.

26. Queutey, P.; Deng, G.B.; Guilmineau, E.; Salvatore, F. A Comparison Between Full RANSE and Coupled RANSE-BEM Approaches in Ship Propulsion Performance Prediction **2013**. *Volume 7: CFD and VIV*. V007T08A026, doi:10.1115/OMAE2013-10366.

27. de Laage de Meux, B.; Audebert, B.; Manceau, R.; Perrin, R. Anisotropic linear forcing for synthetic turbulence generation in large eddy simulation and hybrid RANS/LES modeling. *Physics of Fluids* **2015**, *27*, 035115, [https://doi.org/10.1063/1.4916019]. doi:10.1063/1.4916019.

28. Spille, A.; Kaltenbach, H.J. Generation of Turbulent Inflow Data with a Prescribed Shear-Stress Profile. *DNS/LES Progress and Challenges* **2001**, p. 8.

29.   Mullenix, N.J.; Gaitonde, D.V.; Visbal, M.R. Spatially Developing Supersonic Turbulent Boundary Layer with a Body-Force-Based Method. *AIAA Journal* **2013**, *51*, 1805–1819, [https://doi.org/10.2514/1.J051861]. doi:10.2514/1.J051861.

30.   Weitemeyer, S.; Reinke, N.; Peinke, J.; Hölling, M. Multi-scale generation of turbulence with fractal grids and an active grid. *Fluid Dynamics Research* **2013**, *45*, 061407. doi:10.1088/0169-5983/45/6/061407.

31.   Houtin-Mongrolle, F.; Bricteux, L.; Benard, P.; Lartigue, G.; Moureau, V.; Reveillon, J. Actuator line method applied to grid turbulence generation for large-Eddy simulations. *Journal of Turbulence* **2020**, *21*, 407–433, [https://doi.org/10.1080/14685248.2020.1803495]. doi:10.1080/14685248.2020.1803495.

32.   Tangermann, E.; Klein, M. Controlled Synthetic Freestream Turbulence Intensity Introduced by a Local Volume Force. *Fluids* **2020**, *5*. doi:10.3390/fluids5030130.

33.   Pope, S.B. *Turbulent Flows*; Cambridge university Press, 2000.

34.   Jeong, J.; Hussain, F. On the identification of a vortex. *Journal of Fluid Mechanics* **1995**, *285*, 69–94. doi:10.1017/S0022112095000462.

35.   Di Mascio, A.; Broglia, R.; Muscari, R. On the application of the single-phase level set method to naval hydrodynamic flows. *Computers & Fluids* **2007**, *36*, 868–886. doi:https://doi.org/10.1016/j.compfluid.2006.08.001.

36.   P. Kundu I. Cohen, D.D. *Fluid Mechanics 6th Edition*; Academic Press: London, 2015.

37.   CHOI, K.S.; LUMLEY, J.L. The return to isotropy of homogeneous turbulence. *Journal of Fluid Mechanics* **2001**, *436*, 59–84. doi:10.1017/S002211200100386X.

38.   Ross, S.M. *Introduction to probability and statistics for engineers and scientist*; Academic Press is an imprint of Elsevier, 2014.